Peierls barriers and stresses for edge dislocations in Pd and Al calculated from first principles

J. Hartford, B. von Sydow, G. Wahnström, and B. I. Lundqvist
Department of Applied Physics, Chalmers University of Technology and Göteborg University, S-412 96 Göteborg, Sweden
(Received 18 December 1997; revised manuscript received 11 March 1998)

We report generalized stacking fault (GSF) curves along the [121] and [110] directions for Pd and Al, calculated from first principles. The GSF curves are applied in the classic PN model to calculate Peierls barriers and stresses for the Shockley partials and the unsplit edge dislocations in Pd and Al. The obtained stresses using relaxed GSF curves agree well with experiments. The numerical results are also compared with a recently derived analytical expression for the Peierls stress. The GSF curves have been calculated with a pseudopotential implementation of density functional theory. The accuracy of the method have been tested by calculating values for various stacking fault energies of Al, Ni, Cu, Ag, and Pd which favorably compare with other theoretical and experimental values. [S0163-1829(98)02229-2]

I. INTRODUCTION

Mechanical properties of materials depend on phenomena in a hierarchical structure from atomic up to a macroscopic length scale.[1] Today many atomic-scale phenomena are accessible for study with electron-structure theory. Similarly, the continuum treatment of solids accounts successfully for macroscopic phenomena. However, there is gap in between, which is necessary to bridge in order to theoretically model new materials.

On the microscale dislocations are recognized as key concepts for the understanding of mechanical properties of crystalline solids. The Peierls-Nabarro (PN) model provides a conceptual framework for dislocation structure and energetics,[2–4] but a quantitative agreement with experiments has been lacking and the model has not been thought useful as a predictive tool.[4] The model is essentially a continuum treatment, but the dislocation core, the region of inelastic displacement, is given an approximate atomistic description. The forces in the core, where the atomic-scale discreteness really counts, are currently approximated with the generalized stacking fault (GSF) surface.[5,6] The GSF surface is the interplanar potential energy for sliding one half of a crystal over the other half. Such a potential may nowadays be calculated accurately from first principles. This improved input gives a better ground for analysis and the PN model has lately received increased attention.[7–9]

The possibility of accurate input is provided by the density-functional theory (DFT).[10–12] In this theory the complex many-electron problem is replaced by a simpler one, where a functional of the electron density is minimized. Methodological advancement of DFT together with the increasing performance of computers and numerical methods have made it realistic to assess the present types of questions from first principles.

We report DFT results for both unrelaxed and relaxed GSF curves of Pd and Al along the [121] and [110] crystal directions. The GSF curves are applied in the PN model to Shockley partials and edge dislocations and we discuss the various relaxations that can be used for the GSF curves. Dislocation profiles are calculated, as well as barriers and stresses for dislocation motion. The results for Peierls stresses compare well with experimental values. We also present results for two dissociated partial dislocations. The partials are found to be strongly elastically coupled in their motion and the effect of the interactions on the Peierls barrier is discussed. The applicability of a recent analytical expression for the Peierls stress derived by Joós and Duesbery[8] is also examined.

We choose to study fcc metals for two reasons (i) the experimentally observed dislocations have planar cores and should therefore be favorable cases for the PN model and (ii) good interatomic potentials are available for further atomistic studies.[18] The mechanical strength of close-packed metals is not determined by the intrinsic resistance to dislocation motion but depends on extrinsic obstacles, such as solute atoms and precipitates, which block the motion of the dislocations. In stronger covalent, ionic, and intermetallic crystals the plastic properties are directly dependent on nucleation and mobility of dislocations. The intrinsic mobility is also an important variable for creep behavior.[13]

The GSF surface plays an important role in proposed models for the brittle-ductile transition[14–17] and they can also be used for calibration of model potentials for large-scale simulations[18] and as input to quasicontinuum models.[19]

In the next section we asses the accuracy of the present DFT method in this type of application by calculating values for stacking fault energy (SFE) of the Al, Ni, Cu, Pd, and Ag metals. Stacking faults are local energy minima on the GSF surface. In contrast to the rest of the GSF surface, the energies of these stable configurations can be experimentally measured. The GSF results for Pd and Al are then given in Sec. III and followed by a presentation of the PN model in Sec. IV. The PN model with the GSF data as input is applied to the unsplit edge dislocations, the Shockley partials, and the superposed Shokley partials in Pd and Al in Sec. V. Finally, the obtained dislocation energetics is discussed in Sec. VI.

II. CALCULATION OF STACKING FAULT ENERGIES FROM FIRST PRINCIPLES

Total-energy calculations within DFT using a pseudopotential approximation to replace the core electrons and a

 © 1998 The American Physical Society

plane-wave basis for the valence electrons has become a standard model for solids.[20–23] As SFE's are of the same order as the *a priori* accuracy of the pseudopotential method, it is essential to test the method. For that purpose we have calculated SFE's for some fcc metals, which are compared with experiments and previous calculations. The SFE's have been calculated in two ways. First with the axial next-nearest-neighbor Ising (ANNNI) model[24,25] and secondly with a six atomic-layers thick slab calculation.

All supercell energies have been computed with norm-conserving pseudopotentials[26,27] together with the local-density approximation (LDA) for the exchange and correlation energy of the electrons.[11,28] We refer the reader to Refs. 21–23 for further details of the method and give here only some specifications. The energy integration over the Brillouin zone has been made with a rectangular k-point grid according to the Monkhorst-Pack scheme.[29] This sampling is crucial since energies of different supercells and hence different Brillouin zones are compared. The fictitious temperature for broadening of the electron states was set to 0.25 eV for Al and 0.1 eV for the rest of the metals.

A. ANNNI Calculations of SFE

In the ANNNI model a solid is built by atomic planes with a prescribed stacking sequence and the total energy of the solid is expressed as a sum of coupling energies between the individual planes. The energy sum is truncated at next-nearest-neighboring planes and the needed coupling constants can be calculated from small supercells.

If each plane i is given a ''spin variable'' σ_i with sign depending on the stacking of the $(i+1)$th plane, the total energy may be written as

$$E = J_0 - J_1 \sum_i \sigma_i \sigma_{i+1} - J_2 \sum_i \sigma_i \sigma_{i+2} - J_3 \sum_i \sigma_i \sigma_{i+3} - \ldots, \tag{1}$$

where $\sigma_i = 1$ if the stacking of the $(i+1)$th planes follow the $\ldots ABC \ldots$ stacking and $\sigma_i = -1$ if they follow the $\ldots CBA \ldots$ stacking. The coupling constants are given by the following energy differences:

$$\begin{aligned} J_1 &= \frac{1}{4}E[AB] - \frac{1}{6}E[ABC], \\ J_2 &= \frac{1}{8}E[ABCB] - \frac{1}{6}E[ABC] - \frac{1}{2}J_1, \\ J_3 &= \frac{1}{2}\left(\frac{1}{6}E[ABCACB] - \frac{1}{3}E[ABC] - \frac{2}{3}J_1 - \frac{4}{3}J_2\right), \\ &\vdots \end{aligned} \tag{2}$$

where for example $E[AB]$, represents the energy of a periodic supercell with $\ldots ABAB \ldots$ stacking. When only next-nearest planes are considered J_3 vanishes and the ANNNI model is obtained. To test the convergence of the expansion in Eq. (1) we have calculated J_3 for Al and Pd. Its magnitude is found to be smaller than 0.3 meV, which is about a factor 5 smaller than J_2, which in turn is an order of magnitude smaller than J_1. Consequently, at least for Pd and Al, J_3 can be neglected. The size of J_3 is also comparable to the computational accuracy.

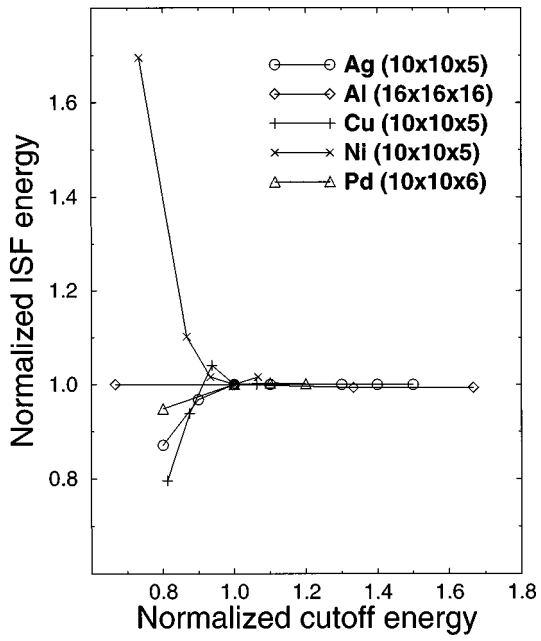

FIG. 1. The figure shows convergence of intrinsic stacking fault energy (ISF) with respect to plane-wave cutoff energy. The axes are normalized to the finally used energy cutoff (given in the legend of Fig. 2) and ISF energies at corresponding cutoffs. The k-point samplings used in the test calculations are given in respective legend.

In the ANNNI model the energies of intrinsic (ISF), extrinsic (ESF), and twin boundary (TWB) stacking fault sequences are given by

$$\begin{aligned} \gamma_{\mathrm{ISF}} &= 4(J_1 + J_2)/A, \\ \gamma_{\mathrm{ESF}} &= (4J_1 + 8J_2)/A, \\ \gamma_{\mathrm{TWB}} &= (2J_1 + 4J_2)/A, \end{aligned} \tag{3}$$

where $A = \sqrt{(3)a_0^2/4}$ is the area per interface atom. For a_0 we use the theoretical value of the equilibrium lattice constants.

The convergence of SFE's with respect to plane-wave energy cutoff is illustrated in Fig. 1. The energies converge well for all metals, although Cu and Ni require high cutoffs. In contrast, the behavior of the different metals is more similar regarding k-point convergence, as seen in Fig. 2, which shows ISF energies calculated with increasingly denser k-point sampling. The grids are made denser in all directions. Previous calculations[17,22] have used a sampling with very high k-point density in the reciprocal direction of [111]. We find that convergence is not achieved until the sampling density is increased in all directions.

The ANNNI results are presented in Table I and compared with experimental values.[4] The calculated data are quite close to the experiments, keeping in mind that the experimental situation is complicated and the uncertainties in the quoted values are quite large, especially for the larger SFE's.

ANNNI results for Al have been reported earlier and we have reproduced the result by Hammer and co-workers,[22]

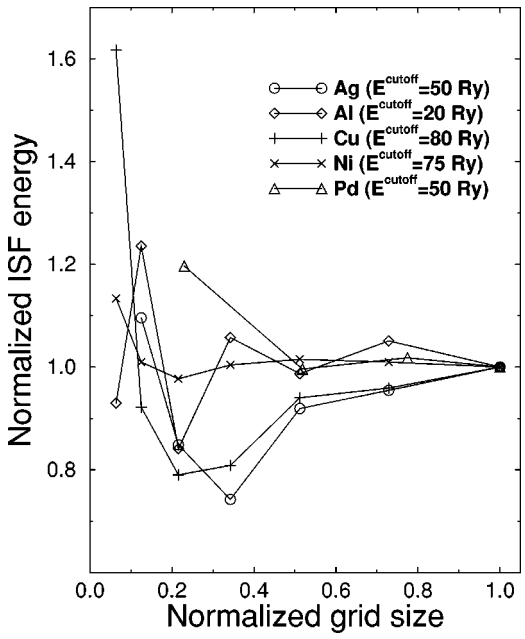

FIG. 2. The figure shows convergence of intrinsic stacking fault energy (ISF) with respect to k-point sampling. The grids range from $6\times6\times3$, $8\times8\times4, \ldots,$ to $20\times20\times10$, except for Pd which start at $12\times12\times8$ and ends at $25\times25\times8$. The axis are normalized to the final sampling and ISF energies. The energy cutoffs are given in respective legend.

$\gamma_{\mathrm{ISF}}=66$ meV/atom$=156$ mJ/m^2, within 1 mJ/m^2 using their energy cutoff and k-point grid, but the present pseudopotential. Our ISF results for Cu and Ag also agree quite well with those of Schweizer and co-workers, who obtained 61 and 24 mJ/m^2 for Cu and Ag, respectively. They used a pseudopotential method with a mixed basis of both plane waves and localized functions.[31]

B. Slab calculations of ISF

The ANNNI model assumes the fault interactions to be short ranged. To estimate the errors due to neglect of J_3 and higher-order terms in Eq. (1) we have calculated ISF energies with a six atomic-layers thick slab calculation. An ISF amounts to sliding one half of the crystal a distance $a_0/\sqrt{6}$ in the [121] direction. This may be accomplished by tilting the [111] supercell vector. With this procedure the fault-fault distance becomes six layers and the ISF is the energy difference between the untilted and tilted supercells. The calculations are made with k-point grids of size $20\times20\times4$ for Cu and $16\times16\times4$ for the rest of the metals and the same plane-wave energy cutoffs as in Sec. II A, except for Al where 15 Ry have been used. This assures a convergence in energy differences at least as good as for the ANNNI energies.

TABLE I. Stacking fault energies (in mJ/m^2) calculated with the ANNNI model for selected fcc metals. Three types of SFE's are given: intrinsic (ISF), extrinsic (ESF), and twin boundary (TWB) stacking fault. The energies are compared with experimental values and for the ISF also with the a six-atomic-layers thick slab.

	γ_{ISF}	γ_{ISF} slab	γ_{ISF} expt.	γ_{ESF}	γ_{TWB}	γ_{TWB} expt.
Ag	29	21	16	29	14	8
Al	161	153	166	147	73	75
Cu	53	51	45	54	28	24
Ni	185	182	125	175	87	43
Pd	192	186	180	178	89	

Our values of γ_{ISF} for the six atomic layer thick slabs are compared to the ANNNI results in Table I. The differences for Ni, Pd, and Cu are within the limits by which J_1 and J_2 are determined. The relative success of the ANNNI model confirms that SF's have a short-ranged influence on the electron structure and that the SFE's are dominated by the structural fcc-hcp (J_1) energy difference.[30] Only for Ag is the ANNNI model relatively less accurate, probably because a large part of the SF is due to the long-ranged free-electron like bonds.[31,32]

Stacking faults have also been calculated with all-electron Green-functions techniques.[30,33] To their advantage, the implementations do not need periodic supercells and in practice, energies for infinite separation of faults may be calculated. The disadvantage is the use of a shape-restricted electron potential, the atomic-sphere approximation (ASA). The ASA treats the interstitial regions between the atoms, important for solids with a relatively high charge density in that region, less well. Due to the ASA the errors are significant for Pd and even larger for Al and Ag.[30]

To summarize, our test shows that, together with the comparison with previous calculations and with experiments, pseudopotential calculations of transition metal SFE's give results with high and sufficient accuracy.

III. GENERALIZED STACKING FAULTS FOR PD AND AL

Next we consider the unrelaxed and relaxed GSF surfaces, $\gamma_{\mathrm{GSF}}(\mathbf{f})$, for Pd and Al on the (111) glide plane. The generalized stacking fault vector $\mathbf{f}$, is the displacement of the upper half-crystal relative to the one below. We have calculated $\gamma_{\mathrm{GSF}}(\mathbf{f})$ along two directions. Figures 3 and 4 show the energetics for sliding along the [121] Shockley partial direction, while Figs. 5 and 6 show the corresponding curves along the [110] edge direction. All fault energies have been computed in the same manner as the slabs in Sec. II B. The full slide along [121] amounts to the ISF given in Table I and the ANNNI ISF energies are shown for comparison in the corresponding figures.

The dependence of the fault-fault interaction on supercell size has been tested by computing the [121] curve with nine layers. The deviations are smaller than 3 mJ/m^2. The curves shown for [110] are mirrored around $f=0.5$, with f in units of $a_0/\sqrt{2}$, since they are periodic. The periodicity has been checked by calculating γ_{GSF} for $f=1$. The errors for Pd and Al are less than 1 and 3 mJ/m^2, respectively. Note that our [121] curves for Al differ from those of Kaxiras and Duesbery,[17] a fact that may be explained by their use of a primitive supercell for the bulk reference, which give a slower k-point convergence.

Relaxation perpendicular to the (111) plane lowers energies considerably and changes the shape of the GSF curves. The relaxations were performed by first optimizing atomic

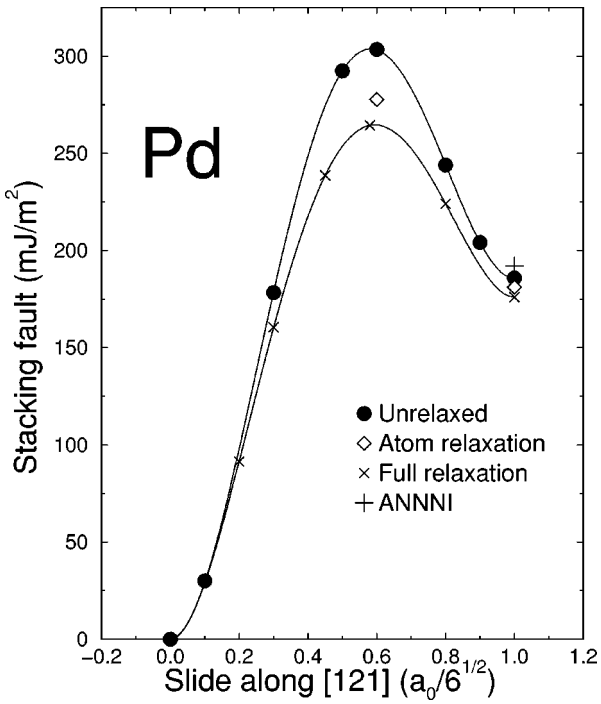

FIG. 3. Generalized stacking fault curve for Pd sliding in the [121] direction on the (111) plane. Figure 7 shows the corresponding Shockley partial Burgers vector for the slide. Relaxations are only allowed perpendicular to the (111) plane. Full relaxation includes optimization of both supercell volume and atomic positions, while atomic relaxation only includes relaxation of the latter. The full slide is the intrinsic stacking fault (ISF) configuration and the six atomic-layers slab curves are compared with the ANNNI value for the ISF given in Table I.

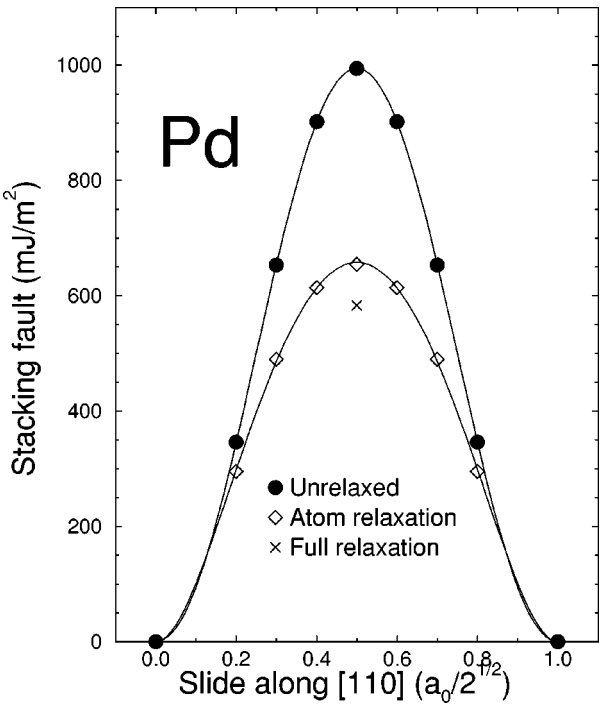

FIG. 5. Generalized stacking fault curve for Pd sliding in the [110] direction on the (111) plane. The slide correspond to the Burgers vector of the edge dislocation shown in Fig. 7. The calculations have been performed in the same manner as for the [121] Shockley partials.

coordinates following the Hellman-Feynman forces (atom relaxation) and secondly by a combined optimization of supercell volume and atomic coordinates (full relaxation). The fully relaxed ISF for Al is 143 mJ/m^2 and for Pd it is 176 mJ/m^2. In the [110] direction the optimal volume expansion is quite large, about 2% at $f=0.5$, but the lowering in

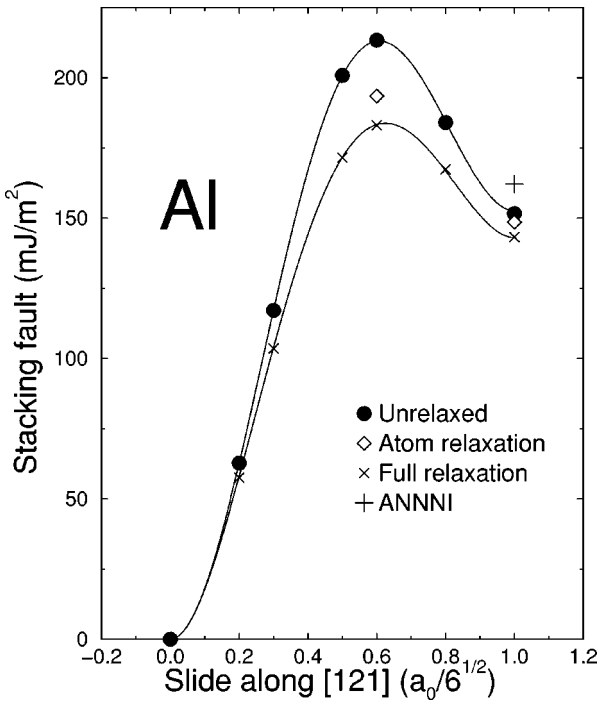

FIG. 4. Same as in Fig. 3, but for Al.

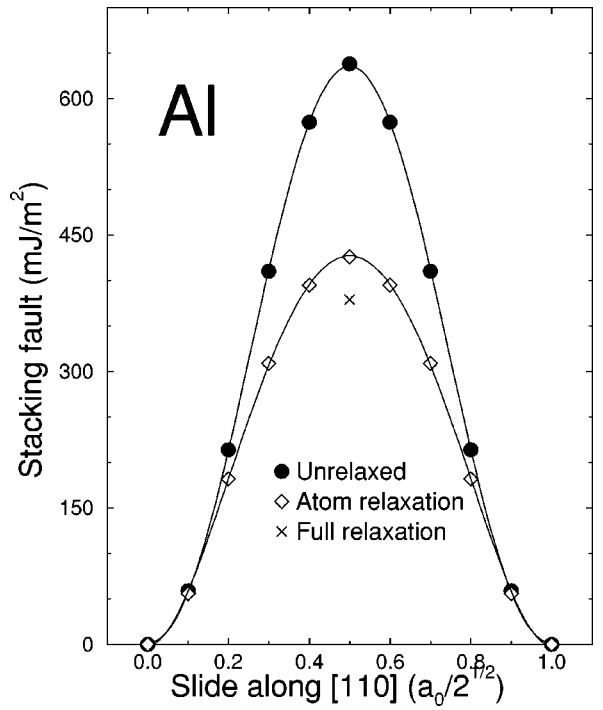

FIG. 6. Same as in Fig. 5, but for Al.

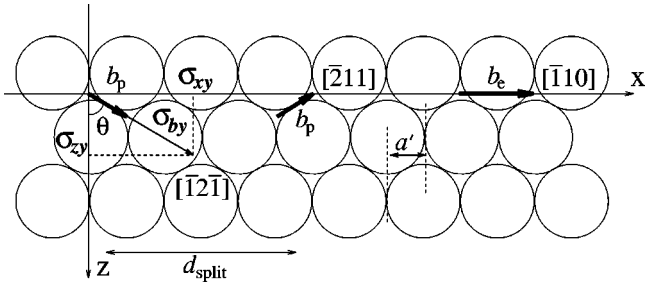

FIG. 7. Geometry of edge dislocations on the fcc (111) plane. To the left, two dissociated Shockley partials (b_p) separated by a stacking ribbon region of width d_{split}. The Burgers vector ($b_p = a_0/6^{1/2}$) of the partial is oriented in the $\langle 121 \rangle$ direction. The unsplit edge dislocation, to the right, has its vector ($b_e = a_0/2^{1/2}$) in the $[\bar{1}10]$ direction. The interplanar spacing in the direction of dislocation sliding (x) is $a' = a_0/(2^{3/2})$.

energy is small compared to only atom relaxation. Such large changes in volume would require modification of the dislocation model to be considered in Sec. V.[9] Therefore, we have only calculated atom relaxed curves in that direction.

IV. PEIERLS-NABARRO MODEL

The classic Peierls-Nabarro (PN) model for planar dislocations provides a continuum solution for the disregistry of the dislocation from which a misfit energy can be computed and thus also energy barriers and stresses for dislocation motion. In the PN model, a dislocation is introduced into a lattice with the assumption that the dislocation core, the region of inelastic displacement, is spread only along the glide plane. We may construct such a dislocation by separating a solid into two halves, inserting the additional lattice planes of the dislocation in the upper half, and then rejoining the two halves. The dislocation generates stresses at the interface/glide plane which in the PN model are calculated according to elasticity theory. The elastic stresses are restored by atomic forces acting on either side of the glide plane due to the misfit of atomic planes. The atomic force may be approximated by the appropriate GSF curve, as originally done by Christian and Vitek.[6] The minimum energy distribution of the dislocation occurs when the elastic and atomic forces balance at each point in the glide plane.

Consider the geometry in Fig. 7. The dislocation line is along the z direction with Burgers vector $\mathbf{b} = b\hat{b} = b\cos\theta\hat{z} + b\sin\theta\hat{x}$. The elastic stress generated in the glide plane ($y = 0$) at a distance x from the dislocation line in the direction of $\hat{b}$ is given by,[4]

$$\sigma_{yb}(x) = \frac{K_b}{2\pi} b \frac{1}{x}, \tag{4}$$

where K_b is an material-dependent elastic constant. For an isotropic medium, $K_b = \mu[(1-\nu)^{-1}\sin^2\theta + \cos^2\theta$, with μ being the the shear modulus and ν Poisson's ratio. Both Pd and Al are, however, anisotropic and one has to resort to the elastic equations appropriate for an anisotropic medium. We have followed the procedure outlined in Refs. 4,34. The required input parameters, c_{11}, c_{12}, and c_{44}, are taken from experimental data[35] and the obtained elastic constants K_b for both a Shockley partial with $\mathbf{b} = a_0/\sqrt{6}(1/2, 0, -\sqrt{3}/2)$ and a edge dislocation with $\mathbf{b} = a_0/\sqrt{2}(1,0,0)$ are given in Table II. The Burgers vectors are given in the Cartesian coordinates of Fig. 7.

TABLE II. Anisotropic elastic constants (in meV/Å^3) for the stress field of the edge and Shockley partial dislocations in Pd and Al.

	Pd edge	Pd partial	Al edge	Al partial
K_b	486.1	433.0	249.3	226.6
K_{split}		296.2		147.3

The restoring atomic force per unit area is approximated by the GSF surface, $\mathbf{F}(\mathbf{f}) = -\nabla\gamma_{GSF}(\mathbf{f})$. Accordingly, in the $\hat{b}$ direction we write

$$F_b(f_b(x)) = -\frac{\partial\gamma_{GSF}(f_b(x))}{\partial f_b}, \tag{5}$$

where $f_b(x)$ denotes the disregistry of the two halves of the crystal in direction $\hat{b}$ as a function of the distance x in the glide direction. The misfit density of the dislocation is related to $f_b(x)$ through

$$\rho_b(x) = \frac{d}{dx} f_b(x). \tag{6}$$

The PN integrodifferential equation is obtained by balancing the elastic stresses caused by the dislocation with the restoring atomic forces:

$$\frac{K_b}{2\pi}\int_{-\infty}^{\infty} \rho_b(x')\,\frac{1}{x-x'}\,dx' = F_b(f_b(x)). \tag{7}$$

To find a misfit energy of the dislocation as a function of position on the x axis, let us say u, the lattice discreteness must be reintroduced. This is obtained in a natural way by summing up the misfit energy only at the positions of the underlying atomic planes[4,38]

$$W(u) = \sum_{m=-\infty}^{+\infty} a'\gamma_{GSF}[f_b(ma'-u)], \tag{8}$$

where a' is the interplanar distance along the sliding direction x. The inelastic part of the energy cost to create a dislocation is the minimum of the misfit energy, $W_{misfit} = \min W(u)$. The stress to overcome the barrier in the misfit energy is

$$\sigma(u) = \frac{1}{b\sin\theta}\frac{dW(u)}{du}, \tag{9}$$

where $b\sin\theta$ is the edge part of the Burgers vector (see the Peach-Kohler formula[4]). The Peierls stress (σ_P) of a dislocation is the maximum of $\sigma(u)$. The corresponding energy barrier (W_P) is the amplitude of $W(u)$.

TABLE III. Inelastic misfit energies (W_{misfit}), Peierls barriers (W_{P}), and stresses (σ_{P}) for a single Shockley partial and an edge dislocation in Pd. The values are computed from the numerical solution of the PN model, Eq. (7). The widths (ξ) of the calculated dislocation profiles is also presented. The Peierls stresses of the numerical solutions are compared with results obtained from the analytical expression in Eq. (11), using the maximum restoring forces ($\tau_{\max}$) from the GSF curves. The isotropic shear modulus (μ) for Pd is 328 meV/Å^3.

	ξ	W_{misfit}	W_{P}	σ_{P}	$\tau_{\max}$	$\chi=\frac{K_b b}{4\pi\tau_{\max}}$	$\sigma_P(\chi)$
	(a')	(meV/Å)	(meV/Å)	($10^{-5}\mu$)	($10^{-2}\mu$)	(a')	($10^{-5}\mu$)
[110] unrel	1.10	275	1.1	280	21.8	1.08	330
Atom rel	1.84	346	0.0013	0.33	14.3	1.65	9.2
[121] unrel	1.30		0.086	42	9.82	1.24	74
Full rel	1.40		0.014	7.0	8.41	1.44	21

A. Analytical solution of PN model

For a sinusoidal form of the restoring force per unit area, $F_b(f)=\tau\sin(2\pi f/b)$, it is possible to solve the PN equation analytically.[36] The solution can be written as

$$f_b(x)=\frac{b}{\pi}\arctan\left(\frac{x}{\xi}\right)+\frac{b}{2}, \tag{10}$$

where $\xi=K_b b/(4\pi\tau)$ is the half width at half maximum of the misfit density of the dislocation. Originally the magnitude of the restoring force τ was deduced from elasticity theory. A more natural definition is, however, to take the maximum slope of the GSF curve, $\tau=\tau_{\max}\equiv\max|\partial\gamma/\partial f_b|$.[8,37] As seen when comparing the present GSF curve for Pd and Al with that of Si in Ref. 38, such a definition is able to capture some of the large differences in chemical bonding, which is not displayed by the elastic constants.

An analytical solution for $\sigma(u)$ with a sinusoidal restoring force was given recently by Joós and Duesbery.[8] For the case of not too narrow dislocations, approximately $\xi/a'>0.5$, they obtained the Peierls stress,

$$\sigma_{\text{P}}(\xi)=\frac{K_b b}{a'}\exp\left(-\frac{2\pi\xi}{a'}\right), \tag{11}$$

where $\xi=K_b b/(4\pi\tau)$. With $\tau=\tau_{\max}$ for Si and Cu in the new expression gives Peierls stresses of correct order of magnitude.[8] The original derivation for the Peierls stress was formally only valid for very wide dislocations.[2,3] In addition, it had an unphysical summation for $W(u)$ and its applicability has been questioned.[4,38] The work of Joós and Duesbery have therefore restored credibility to the PN model and to the analytical expression for the Peierls stress in Eq. (11).

B. Numerical solution of PN model

When solving the PN equation one can make use of the analytical expression in Eq. (10).[38–40] We use a recent ansatz proposed by Gan and Jang,[41]

$$f_b(x)=\frac{b}{\pi}\sum_i \alpha_i\left[\arctan\left(\frac{x-x_i}{c_i\xi_i}\right)+(1-c_i)\,\frac{\xi_i(x-x_i)}{x^2+(c_i\xi_i)^2}\right]+\frac{b}{2}. \tag{12}$$

The normalization of f_b, $\int_{-\infty}^{+\infty}\rho_b(x)dx=b$, requires that $\Sigma_i\alpha_i=1$. It is customary to restrict α_i to non-negative values in order to allow the ansatz (12) to be interpreted as a sum of partial dislocation. This interpretation is not called for here and to obtain good solutions for the [121] cases, which are asymmetric in $F_b(f_b)$, negative α_i's are allowed. For the same reason we chose two sets of $\xi=K_b b/(4\pi\tau)$ using maximum positive [$\tau=\max(\partial\gamma/\partial f_b)$] and negative restoring force [$\tau=|\min(\partial\gamma/\partial f_b)|$]. Inserting the ansatz in both sides of Eq. (7) reduces the integrodifferential equation to a set of nonlinear equations in the parameters α_i, x_i, and c_i which are solved in a least-squares sense.

V. EDGE DISLOCATIONS IN PD AND AL

The PN equation [Eq. (7)] is solved numerically using the above ansatz for the disregistry. We use unrelaxed and relaxed GSF curves and consider both the unsplit edge and a single partial. Dislocation widths, misfit energies, Peierls barriers, and stresses are calculated from the numerically obtained disregistries as described in the previous section.

A. Unsplit edge

Although the unsplit edge is not observed experimentally in Pd or Al it is interesting to compare the outcome of the PN model for that dislocation with the corresponding results for the ordinary partials. The symmetric GSF curve also allows for a more fair comparison of the analytical expression in Eq. (11) with the the full solution.

Tables III and IV gives the PN model results for the edge dislocations. The relaxed GSF curves are lowered and flattened and restoring forces are thus reduced and the dislocations become broader. The lowering of the GSF curves are carried over to $W(u)$ and together with the broadened disregistry the Peierls barriers and stresses become much smaller. This illustrates the sensitivity of the barrier on the maximum restoring force $\tau_{\max}$, expressed by the exponential dependence in Eq. (11). The misfit energy for the relaxed Pd edge is higher than for the unrelaxed. This may suggest that the relaxations of the GSF surface are incompatible when used for individual lattice planes in the PN model. That is, the separate relaxation of the GSF surface and solution of the

TABLE IV. Same as Table III, but for Al. The isotropic shear modulus (μ) for Al is 165 meV/Å^3.

	ξ (a')	W_{misfit} (meV/Å)	W_{P} (meV/Å)	σ_{P} ($10^{-5}\mu$)	$\tau_{\max}$ ($10^{-2}\mu$)	$\xi=\frac{K_b b}{4\pi\tau_{\max}}$ (a')	$\sigma_{\text{P}}(\xi)$ ($10^{-5}\mu$)
[110] unrel	0.87	163	2.6	1250	27.3	0.88	1200
Atom rel	1.51	159	0.015	7.1	17.9	1.34	65
[121] unrel	1.17		0.12	110	13.0	0.97	410
Full rel	1.49		0.0090	8.5	10.9	1.16	130

PN equation does not yield the variational energy minima solution, but instead solutions with too low barriers.

As seen in Figs. 5 and 6 the unrelaxed GSF curves are close to sinusoidal. Hence, the numerical solution is close to the analytical solution in Eq. (11). The dislocation widths (ξ) and Peierls barriers are compared in Tables III and IV. The deviation from the sinusoidal form due to relaxation reduces the good agreement.

B. Shockley partial

Experimentally observed edge dislocations in fcc metals split and form an ISF ribbon bounded by two Shockley partials. For Al the splitting distance (d_{split} in Fig. 7) is small and the individual partials are overlapping. When the PN equation is solved for a single partial the summation in $W(u)$ includes an arbitrary long ISF. This gives a constant shift in the misfit energy that vanishes for $\sigma(u)$. Results for the dislocation energetics are presented in Tables III and IV. The effect of relaxation is smaller than for the edge dislocations, but still large.

Tables III and IV also presents results for the analytical expression using $\xi=K_b b/(4\pi\tau_{\max})$. The discrepancy between the analytical and numerical solution follows from the asymmetry in γ_{GSF}, which increases with relaxation, especially for Al.

C. Superposed Shockley partials

To study a complete split edge the solutions for the single partials are superposed. This may be warranted for Pd where the splitting of the partials is quite large, that is, the partial cores should not overlap too much. For Al this is more questionable, but the procedure should at least give a picture of the dislocation structure and an estimate for the barriers.

The equilibrium splitting of two partials is a balance between the gain in elastic energy and the cost of ISF energy. Elasticity theory gives the equilibrium separation[4]

$$d_{\text{split}}=\frac{b^2 K_{\text{split}}}{2\pi\gamma_{\text{ISF}}}, \tag{13}$$

where b is the partial Burgers vector. The elastic constant K_{split} is composed of a repulsive edge and an attractive screw part. It is obtained from the anisotropic elastic equations in the same manner as K_b and given in Table II.

Depending on the elastic coupling the two partials may move separately or together and the misfit energy in Eq. (8) is appropriately written as

$$W(u_1,u_{\text{r}})=\sum_{m=-\infty}^{+\infty} a'\,\gamma_{\text{GSF}}[f_{\text{l}}(ma'-u_{\text{l}})+f_{\text{r}}(ma'-u_{\text{r}})], \tag{14}$$

where u_{l} and u_{r} is the position of the left and right partial, respectively. If the coupling is strong it is possible to have a situation where one partial moves up on the energy barrier, while the other moves downwards, hence lowering the total barrier.[44] Whether one partial is on top of the barrier or both are in an energy minimum position will depend on the splitting distance used for the superposition. As it is not possible to find the exact equilibrium distribution on the underlying lattice nor the exact elastic interaction within the present PN model we chose d_{split} to be an integer times a' close to the approximate equilibrium distance given by Eq. (13). This gives a distribution of planes in W for the superposed partials similar to the single ones. The splitting distance for Pd is $8a'$ and $5a'$ for Al. The two partial cores in Pd are fairly separated (Fig. 8), but are overlapping in Al (Fig. 10).

Figures 9 and 11 show the relaxed misfit energy, $W(u_{\text{l}},u_{\text{r}})$, for Pd and Al. In both metals the minimum energy barrier is along a very narrow valley on the diagonal ($u_{\text{l}}=u_{\text{r}}$). Thus, the partials are strongly coupled and move simultaneously. The misfit barriers for the unrelaxed dislocations are larger but still close to the diagonal. Values for Peierls energies and stresses for both unrelaxed and relaxed superposed partials are given in Table V. Even though the Peierls barrier is lower for the relaxed edge, the misfit energies are much lower for the split dislocation, which make

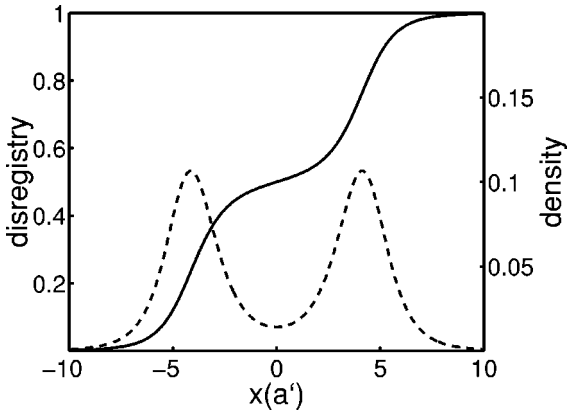

FIG. 8. Disregistry, $f_b(x)$, and dislocation density, $\rho_b(x)$, for two superposed Shockley partials in Pd. The single partials are solutions for the relaxed γ_{GSF} curves. The separation between the partials is chosen to be $8a'$.

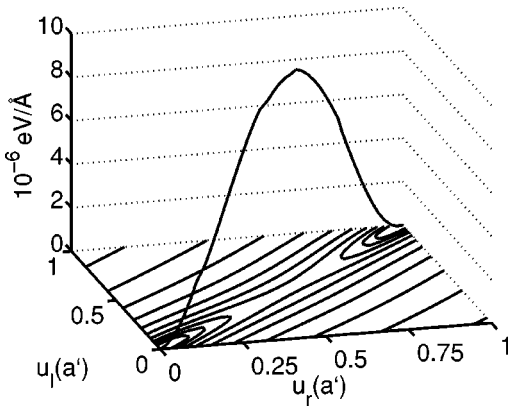

FIG. 9. Misfit energy for two superposed Shockley partials in Pd. The contour plot shows the misfit energy, $W(u_l,u_r)$, as a function of relative position on the glide plane of the left partial (u_l) and the right partial (u_r). The 3D curve illustrates the energy barrier for the minimum energy path. The innermost contour corresponds to $W=1.5\times10^{-6}$ eV and the following are doubled in energy. The minimum energy path lies on the diagonal and its valley is very narrow, which means that the partials are strongly elastically coupled.

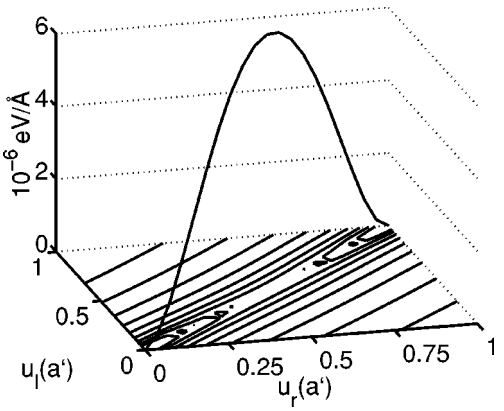

FIG. 11. Same as in Fig. 9, but for Al. The innermost contour corresponds to $W=3\times10^{-6}$ eV and the following are doubled in energy. Similar to Pd, the Al partials are also strongly elastically coupled.

them energetically favorable. Similar behavior is also observed for $\langle110\rangle\{111\}$ dislocations in Si.[38] The obtained Peierls stresses for the relaxed partials are close to experimental measurements, which report stresses for fcc metals of the order $1-5\times10^{-5}\mu$.[42,43]

VI. DISCUSSION AND CONCLUSIONS

A striking effect is the huge change in Peierls barriers when the $\gamma_{\mathrm{GSF}}(\mathbf{f})$ is allowed to relax. A full atomistic simulation would include more degrees of freedom and the barriers may therefore be further reduced. This implies that the PN stresses are too small, since the obtained stresses are already close to the experimental results. The low barriers may be a result of the separate relaxation of the GSF surface and solution of the PN equation not yielding the variational energy minima solution.

Recent work by Bulatov and Kaxiras[9] includes a semidiscrete and variational method for the relaxation of the GSF surface when solving for the core structure and Peierls barrier. Their approach, when applied to the $\langle110\rangle\{111\}$ glide screw in Si, gives a Peierls barrier two order of magnitudes lower than that obtained with an unrelaxed GSF curve using the classic PN model. This Si glide-set dislocation is very narrow and the effects of the improved model likely to be smaller for the much wider dislocations in Pd and Al. [Joós and Duesbery applied Eq. (11) to the wider shuffle set.] However, including more degrees of freedom must reduce the barriers compared to present unrelaxed results, but not necessarily below the fully relaxed barriers since they not are variationally obtained. The new approach also includes elastic displacement perpendicular to the glide plane and the gain in misfit energy from the volume relaxation of the GSF curve is reduced by the cost of elastic energy. From slab calculations for Pd and Al the reduction is estimated to be about 50%. It seems plausible that the variational approach results in barriers in between present unrelaxed and fully relaxed solutions, which would form realistic upper bonds on the Peierls barriers.

We believe the present implementation of DFT to give values of high and sufficient accuracy. Atomistic simulations also show that the superposition of single partials, and only allowing a disregistry along one direction and not on the whole of the GSF surface, are justified simplifications.[18] Another concern is the use of linear theory of elasticity to calculate the stresses in the left-hand side of the PN equation

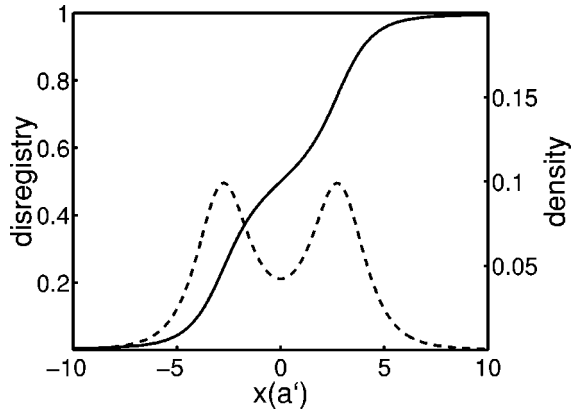

FIG. 10. Same as in Fig. 8, but for Al. Here the separation between the partials is chosen to be $5a'$.

TABLE V. Inelastic misfit energies (W_{misfit}), Peierls barriers (W_{P}), and stresses (σ_{P}) for two superposed Shockley partials, forming a stacking fault ribbon and a complete edge dislocation (see Fig. 7), in Pd and Al. The splitting distance (d_{split}) of the partials, or rather the approximate width of the ribbon, is chosen to be $8.0a'$ for Pd and $5.0a'$ for Al.

	W_{misfit} (meV/Å)	W_{P} (meV/Å)	σ_{P} ($10^{-5}\mu$)
Pd unrel	209	0.094	27
Full rel	189	0.0099	3.4
Al unrel	113	0.13	67
Full rel	111	0.0070	3.3

[Eq. (7)] (Ref. 45) and further atomistic simulations are needed in order to clarify the quality of the core structure predicted by the PN model.[18]

Measurements of internal friction resonance, the so called Bordoni peak, in close-packed metals yields an ''internal stress'' two order of magnitude greater than the Peierls stress obtained from yield stress data.[46] The elastic coupling can reduce the barriers as described in Sec. V C and have been suggested to be the reason for the observed differences in measured stresses.[44] Even if present theoretical values have to be reconsidered with more appropriate account for the relaxation of the GSF curves the already low barriers for the single partials are not likely to increase by order of magnitudes. The elastic coupling is evidently not the cause of the discrepancy in measured stresses. However, the coupling can make the total barrier sensitive to local values of elastic constants and ISF energies due to presence of vacancies and impurities, which could explain the broad spectra of measured Peierls stress of an individual metal.[44] Bulatov's and Kaxiras' improved PN model[9] also addresses the neglect of changes in core structure during motion. It would be interesting to study the sensitivity in Peierls stress due to elastic coupling with such a PN model.

As expected, $\tau_{\max}$ is playing a major role for the Peierls stress. Hence, the analytical expression [Eq. (11)] is able to give present trends, but a single input parameter does not suffice quantitatively when the GSF curve deviate from the sinusoidal form. To judge the usefulness of the expression, a test against a larger set of data and a settlement about the validity of the present PN model is necessary.

In summary, besides being an important conceptual tool the classic PN model also includes some quantitative capabilities. Presently the latter should be termed semiquantitative as there is room for improvements even for the supposedly favorable fcc metal case. A case which is suitable for a thorough analysis of both the elastic and atomistic parts of the PN model and future efforts will focus on detailed comparisons between the model and full atomistic simulations.

ACKNOWLEDGMENTS

This work has been supported by the Swedish Board for Industrial and Technical Development and the Swedish Natural Science Research Council. The DFT calculations have been performed with a computer code developed by Hammer (Ref. 47). We are thankful to U. Engberg for his assistance with some of the DFT calculations for the ANNNI model parameters. We have also benefited from discussions with H. O. Andrén.

[1] A. Kelly, *Strong Solids*, 2nd ed. (Oxford University Press, Oxford, 1973).
[2] R. E. Peierls, Proc. Phys. Soc. London **52**, 23 (1940).
[3] F. R. N Nabarro, Proc. Phys. Soc. London **59**, 256 (1947).
[4] J. P. Hirth and J. Lothe, *Theory of Dislocations*, 2nd ed. (Wiley, New York, 1982).
[5] V. Vitek, Philos. Mag. **18**, 773 (1968).
[6] J. W. Christian and V. Vitek, Rep. Prog. Phys. **33**, 307 (1970).
[7] L. B. Hansen, K. Stokbro, B. I. Lundqvist, K. W. Jacobsen, and D. M. Deaven, Phys. Rev. Lett. **75**, 4444 (1995).
[8] B. Joós and M. S. Duesbery, Phys. Rev. Lett. **78**, 266 (1997).
[9] V. V. Bulatov and E. Kaxiras, Phys. Rev. Lett. **78**, 4221 (1997).
[10] P. Hohenberg and W. Kohn, Phys. Rev. **136**, B864 (1964).
[11] W. Kohn and L. Sham, Phys. Rev. **140**, A1133 (1965).
[12] R. Jones and O. Gunnarsson, Rev. Mod. Phys. **61**, 689 (1989).
[13] W. Blum, *Materials Science and Technology*, edited by R. W. Cahn, P. Haasen, and E. J. Kramer (VCH, Berlin, 1992), Vol. 6.
[14] E. Kaxiras and M. S. Duesbery, Phys. Rev. Lett. **70**, 3752 (1993).
[15] S. J. Zhou, A. E. Carlsson, and R. Thomson, Phys. Rev. Lett. **72**, 852 (1994).
[16] R. Thomson, Phys. Rev. B **52**, 7124 (1995).
[17] Y. Sun and E. Kaxiras, Philos. Mag. A **75**, 1117 (1997).
[18] B. von Sydow, J. Hartford, and G. Wahnström (unpublished).
[19] B. E. Tadmor, M. Ortiz, and R. Phillips, Philos. Mag. A **73**, 1529 (1996).
[20] M. T. Yin and M. L. Cohen, Phys. Rev. B **25**, 7403 (1982).
[21] M. C. Payne, M. P. Teter, D. C. Allen, T. A. Arias, and J. D. Joannopoulos, Rev. Mod. Phys. **64**, 1045 (1992).
[22] B. Hammer, K. W. Jacobsen, V. Milman and M. C. Payne, J. Phys.: Condens. Matter **4**, 10 453 (1992).
[23] G. Kresse and J. Furthmüller, Phys. Rev. B **54**, 11 169 (1996).
[24] P. J. H. Denteneer and W. van Haeringen, J. Phys.: Condens. Matter **20**, L883 (1987).
[25] P. J. H. Denteneer and J. M. Soler, Solid State Commun. **78**, 857 (1991).
[26] N. Troullier and J. L. Martins, Phys. Rev. B **43**, 1993 (1991).
[27] G. B. Bachelet, D. R. Hamann, and M. Schlüter, Phys. Rev. B **26**, 4199 (1982).
[28] J. P. Perdew and A. Zunger, Phys. Rev. B **23**, 5048 (1981).
[29] H. J. Monkhorst and J. D. Pack, Phys. Rev. B **13**, 5188 (1976).
[30] N. M. Rosengaard and H. Skriver, Phys. Rev. B **47**, 12 865 (1993).
[31] S. Schweizer, C. Elsässer, and M. Fähnle, Phys. Rev. B **48**, 14 706 (1993).
[32] S. Schweizer, C. Elsässer, K. Hummler, and M. Fähnle, Phys. Rev. B **46**, 14 270 (1992).
[33] S. Crampin, K. Hampel, D. D. Vvedensky, and J. M. MacLaren, J. Mater. Res. **5**, 2107 (1990).
[34] L. J. Teutonico, Acta Metall. **11**, 1283 (1963).
[35] Compiled by P. Eckerlin and H. Kandler, *Landolt-Börnstein, Numerical Data and Functional Relationships in Science and Technology*, edited by K.-H. Hellwege, (Springer-Verlag, Berlin, 1971).
[36] J. D. Eshelby, Philos. Mag. **40**, 903 (1949).
[37] J. J. Gilman, Science **261**, 1436 (1993).
[38] B. Joós, Q. Ren, and M. S. Duesbery, Phys. Rev. B **50**, 5890 (1994).
[39] A. J. E. Foreman, M. A. Jawson, and J. K. Wood, Proc. Phys. Soc. London, Sect. A **64**, 156 (1951).
[40] F. Kroupa and L. Lejĉek, Czech. J. Phys. **22**, 813 (1972).
[41] Yong X. Gan and Bor Z. Jang, J. Mater. Sci. Lett. **15**, 2044 (1996).

[42] W. J. McG. Tegart, *Elements of Mechanical Metallurgy* (Macmillan, New York, 1966).
[43] J. N. Wang, Mater. Sci. Eng., A **206**, 259 (1996).
[44] G. Schoeck and W. Püschl, Mater. Sci. Eng., A **189**, 61 (1994).
[45] S. J. Zhou, A. E. Carlsson, and R. Thomson, Phys. Rev. B **49**, 6451 (1994).
[46] G. Fantozzi and C. Esnouf, J. Phys. (Paris) **9**, 557 (1983).
[47] DACAPO version 1.18, Center for Atomic Scale Materials Physics (CAMP), Denmarks Technical University, 1996.